Carbon 207 (2023) 116–128

Contents lists available at ScienceDirect

Carbon

journal homepage: www.elsevier.com/locate/carbon

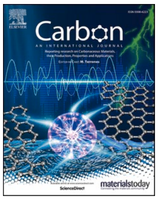

New architecture of 3D graphene with enhanced properties obtained by cold rolling

Vamsi Krishna Reddy Kondapalli [a], Guangqi Zhang [a], Yu Zhang [a], Mahnoosh Khosravifar [a], Kyle Brittingham [b], Nhat Phan [b], Sergey Yarmolenko [c], Je- Hyeong Bahk [a], Vesselin Shanov [a,b,*]

[a] *Department of Mechanical and Materials Engineering, University of Cincinnati, Cincinnati, OH, 45221, USA*
[b] *Department of Chemical and Environmental Engineering, University of Cincinnati, Cincinnati, OH, 45221, USA*
[c] *Engineering Research Center for Revolutionizing Biomaterials, North Carolina A&T State University, IRC Building, Suite 242, Greensboro, NC, 27411, USA*

ARTICLE INFO

Keywords:
3D Graphene
CVD
Additive manufacturing
Cold rolling
dry etch
Welding
Hard masks
Reactive ion etching (RIE)

ABSTRACT

Previously, we reported 3D Shaped 3D Graphene ($3D^2G$) with controlled structural design. In this work, we introduced cold rolling as a post-processing technique to obtain compressed $3D^2G$, referred here as $C3D^2G$, and investigated the relationship between its microstructure and properties. The performed comprehensive materials characterization of $C3D^2G$ revealed the micro-motion of the graphene flakes from their random orientations into a stacked and aligned structure along with the extrusion of bulk material into the structural pores which acted as stress-relief spaces. The obtained new bulk morphology significantly enhanced its properties. The achieved gravimetric density, electrical conductivity, and tensile strength of $C3D^2G$ were higher than $3D^2G$ by 37.3, 53.4, and 24.9 times, respectively. A new process was demonstrated based on the observed extrusion enabling the welding of multiple pieces of $3D^2G$ into one structure via cold rolling, thus showing potential for dimensional scaling up. The conducted tensile and electrical conductivity studies across the welded region revealed the presence of a mechanical bond within the joined area with a higher strength than the initial pieces involved in welding. Further, a unique application of this material was explored as a reusable, etch-resistant hard mask for patterning silicon wafers, and as a protective barrier against fluorine plasma environment. The etch rate measurements showed a higher etching resistance of $C3D^2G$ compared to Si and SiO_2 when exposed to a fluorine plasma Reactive Ion Etching (RIE).

1. Introduction

Recently, numerous versions of free-standing 3D graphene synthesized using a wide variety of approaches were reported with extraordinary properties. These structures can be divided into two major groups: joint 3D graphene constructs where the individual graphene flakes are connected through secondary bonding or a second phase, and seamlessly linked 3D graphene networks with carbon atoms interconnected via chemical bonds [1,2]. Joint 3D graphene constructs include graphene aerogels, graphene hydrogels, and graphene-polymer composites which are usually synthesized via hydrothermal, freeze-drying, or additive manufacturing. Most of them possess high strength but reveal poor electrical properties due to the random distribution of pores, presence of functional groups or second phase, and formation of secondary bonds between the flakes [1,3–6].

On the other hand, seamlessly connected 3D graphene networks synthesized via Chemical Vapor Deposition (CVD) exhibit high porosity, reasonable strength, and increased electrical conductivity, which makes them a better fit for sensors and energy storage [7–12]. The pristine nature of these materials enables tuning their properties by creating defects and replacing the carbon atoms with hetero atoms [13,14]. Nonetheless, seamlessly connected 3D graphene networks face production scaling issues caused by the size of the CVD reactors and by the catalyst preparation procedures. Though 3D graphene fabrication using cast or 3D printed catalysts demonstrated customization, it yields a material with poor strength and is limited by the reactor size [7,8].

Numerous post-processing techniques were explored to enhance the properties of 3D Graphene. Thermal reduction, thermal annealing, etc., were explored which resulted in enhanced electrical properties of joint 3D graphene constructs. An increase in electrical conductivity was observed either because of the synergetic effect between the rise in the C/O ratio and the shrinkage to smaller pore structures or due to an

---

* Corresponding author. Department of Mechanical and Materials Engineering, University of Cincinnati, Cincinnati, OH, 45221, USA.
E-mail address: vesselin.shanov@uc.edu (V. Shanov).

https://doi.org/10.1016/j.carbon.2023.03.004
Received 21 November 2022; Received in revised form 20 January 2023; Accepted 3 March 2023

increase in the graphene-to-polymer weight ratio [15,16]. It must be noted here that post-processing of joint 3D graphene constructs enhances some specific properties by compromising other properties. For example, annealing and thermal reduction degrade the structural properties to achieve better electrical conductivity [1,2,6,17]. Surface or bulk modification of seamlessly connected 3D graphene networks using functional groups or second phase achieved via atmospheric plasma functionalization and hydrothermal/solvothermal techniques can increase their hydrophilic nature or surface area but failed to enhance the electrical and mechanical properties [18–20].

Many resistive and piezoresistive sensors use the correlation between the electrical conductivity and deformation of the pores in the 3D graphene as a strategy to quantify motion, vibration, pressure, stress, and strain. The deformed pores increase the contact area thus shortening the electron transfer path and lowering the electrical resistance of the sensor [21–23]. We observed a similar phenomenon in our $3D^2G$ where an increase in the infill density caused a rise in electrical conductivity due to the reduction of the structural pore size [7]. Further, highly porous graphene foam composite was used as a thermal switch by regulating the heat flux via simple compression and relaxation of the material thus altering the contact area by a temporary suppression of the pores [24]. It is obvious from the discussed above-mentioned studies that a temporary or permanent decrease of the porosity in 3D graphene would enhance its electrical and thermal properties.

Various characterization tools like in situ and ex-situ Raman, and X-Ray Diffraction (XRD) have been used to study the deformation mechanism in graphene, few-layer graphene, and graphite under stress [25–29]. Similarly, Molecular Dynamic Simulation (MDS) and Scanning Electron Microscopy (SEM) studies on the deformation mechanism of graphene foam under stress have been reported [30–33]. To the best of our knowledge, a detailed material's characterization of microporous pristine 3D graphene under compression and the effect of this treatment on various properties has not been fully explored. A better understanding of the effect of stress on microstructure and properties of 3D graphene is needed to fully employ its properties for advanced applications.

Here, we introduce cold rolling as a post-processing technique to process 3D Shaped 3D Graphene ($3D^2G$) which results in the formation of its compressed form i.e. Compressed 3D Shaped 3D Graphene ($C3D^2G$). The major goals of this work are to alter the architecture of $3D^2G$ and enhance its properties by cold rolling. The expectation was that by changing the gap between the rollers, the $C3D^2G$ thickness of the obtained graphene materials and their pore size could be tuned. The electrical and mechanical properties were expected to be enhanced with an increase in compression. A wide range of material characterization techniques were employed in pursuit of understanding and highlight the relationship between microstructure, properties, and applications of cold-rolled 3D graphene. In addition, scale-up fabrication and advanced application of $C3D^2G$ as a hard mask and protective material when exposed to harsh corrosive RIE environment were presented here.

2. Experimental section

2.1. Materials and synthesis of $3D^2G$

A detailed procedure describing the synthesis of $3D^2G$ can be found in our previous publication [7]. In brief, nickel-PLGA slurry was prepared by mixing 8.9 g of nickel (Ni) powder (Alfa Aesar, 3–7 μm particle size and 1.8–2.7 g/cm^3 apparent density), 7.5 ml of Dichloromethane (DCM, Fisher Scientific), 0.76 ml of Dibutyl Phthalate (DBP, Sigma Aldrich), and 0.56 g of Poly lactic-co-glycolic acid (PLGA, PolySciTech, L/G 85/15, MW 65,000–75,000 Da), followed by stirring and vortexing to accelerate the DCM evaporation. 3D printable designs were developed using GCode editor/a CAD software/conversion of an image to a CAD/GCode file. The designs were loaded to the Allevi Bioprint software, and the slurry was 3D printed through a 430 μm stainless-steel blunt needle at a printing speed of 6–10 mm/s using an Allevi 2 bioprinter. 3D printed Ni-PLGA structures were used as catalysts for CVD synthesis of $3D^2G$ followed by nickel removal in an HCl bath (15 M at 70 °C). The latter procedure was conducted for at least 12 h to eliminate Ni, which was confirmed analytically, then followed by rinsing with DI water and ethanol. The obtained $3D^2G$ was placed between two Kim wipes to dry. Details related to the materials characterization of this material are presented in the Supplementary Information.

3. Results and discussion

3.1. Response of $3D^2G$ to cold rolling compression

Various 3D printed nickel-PLGA structures with 50% (solid Ni), 40%, and 30% rectilinear infill consisting of 1 or 4 layers were used as catalysts precursors to synthesize $3D^2G$ samples via CVD. The average thickness of $3D^2G$ with 4-layers and 1-layer was 585.7 μm and 150.6 μm respectively as measured by SEM. As shown in Fig. 1, the obtained $3D^2G$ was cold rolled between two thin stainless-steel shims (75 μm in thickness each) at room temperature in a dry ambient environment and was not assisted by any liquid. After rolling compression, the acquired sandwich of $C3D^2G$ laminated between two Stainless Steel (SS) shims was dipped in an ethanol bath for 1 min followed by separation and drying at 50 °C among Kimwipes sheets which resulted in obtaining a freestanding $C3D^2G$. The thickness of the $C3D^2G$ was controlled by changing the gap between the rollers.

The influence of the infill %, the number of 3D printed layers, and the gap between the rollers on the response of $3D^2G$ to compressive stress was studied here. $3D^2G$ samples with 30%, 40%, and 50% infill consisting of 1 and 4 layers, were compressed using different roller gaps.

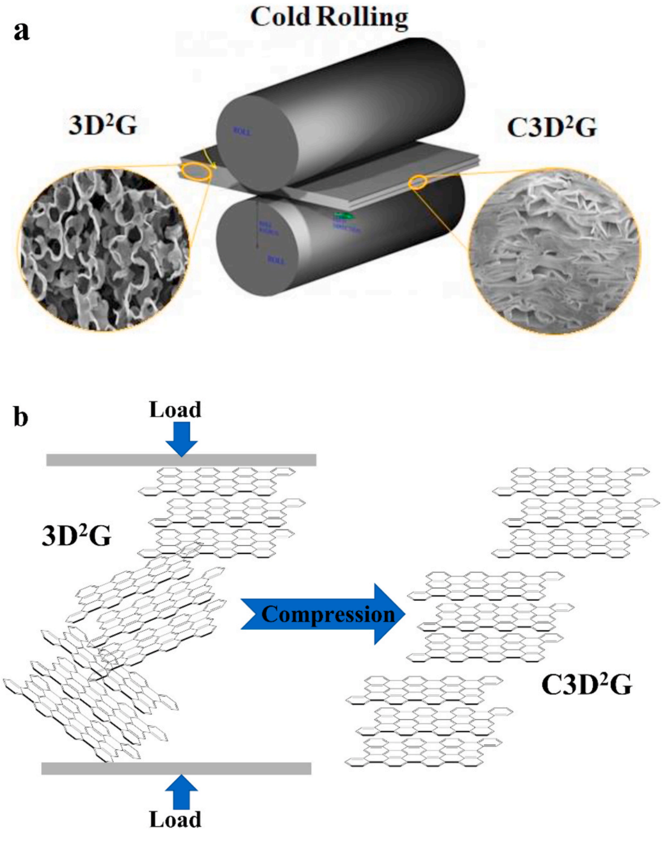

Fig. 1. (a) Overview of the rolling compression procedure used to create $C3D^2G$ from $3D^2G$. Cross-sectional SEM image of $3D^2G$ on the left and SEM image of $C3D^2G$ on the right. (b) Illustration of microstructure before and after compression. (A colour version of this figure can be viewed online.)

The average thickness of the resultant C3D^{2}G was measured and displayed in Fig. 2a along with the gap between the rollers and the expected thickness of C3D^{2}G calculated by the simple equation: expected thickness = rolling gap – 2 x thickness of a SS shim. It was evident that the actual thickness after compression deviated from the expected thickness. When using the 270 μm rolling gap, the actual thickness of 30% and 40% infill C3D^{2}G was lower than the expected thickness. This trend changed when the rolling gap was decreased to 185 μm and 155 μm, where the actual thickness was higher than the expected thickness.

Further, at 155 μm rolling gap, solid 4-layer 3D^{2}G showed higher resistance to compression, pronounced stiffness, and structural cracks along with excessive deformation at the corners were evident. However, the 30% and 40% infill C3D^{2}G samples were flexible and did not display any structural cracks at the same rolling gap after compression. Moreover, the SS shims seemed deformed when used to compress the solid samples at a 155 μm gap where no deformation of SS shims was observed after compression of 30% and 40% infill samples. With any further decrease in the rolling gap, the 30% and 40% infill C3D^{2}G exhibited structural cracks and wrinkles. In contrast to the solid 4-layer 3D^{2}G, the 1-layer solid 3D^{2}G showed no resistance to compression, resulting in a thickness of 6.35 μm at the same roller gap (155 μm), whereas the thickness of the 4-layer solid C3D^{2}G reached only 25.3 μm.

It is clear from the above discussion that the large compressive stress applied via cold rolling induced substantial plastic deformation of 3D^{2}G irrespective of the infill % and the number of layers. After compression at a 155 μm rolling gap, all the samples exhibited a shiny appearance like an aluminium foil, as shown in Fig. 2b. Further, partial structural relaxation (partial compressive strain recovery) was observed here due to the viscoelastic behavior of 3D^{2}G resulting in higher actual thickness than expected. These experimental observations in our work aligned well with the findings of a Molecular Dynamic Simulation (MDS) study from the literature [32]. The authors there found that minimal uniaxial stress applied on randomly aligned graphene flakes resulted in 100% strain recovery, whereas large uniaxial loading caused high plastic deformation with minor strain recovery due to viscoelastic behavior.

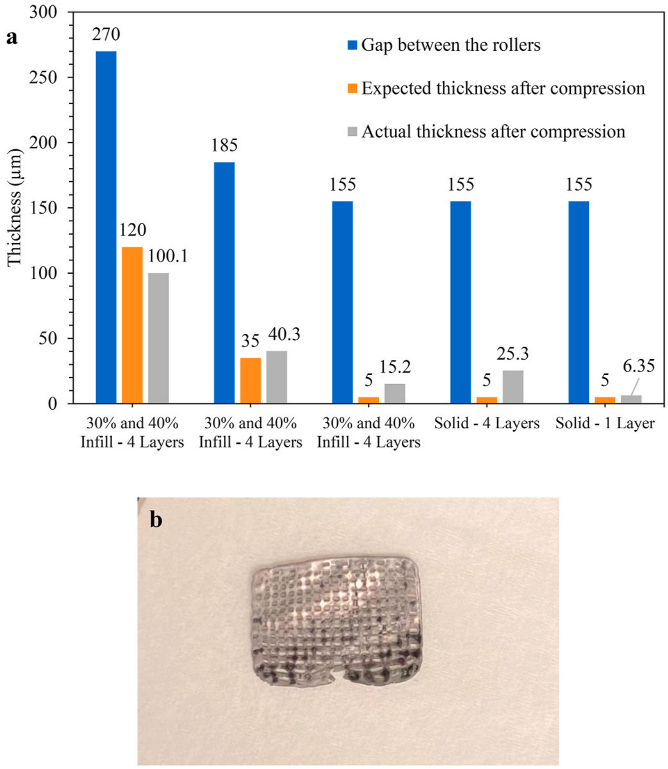

Fig. 2. (a) Bar chart summarizing the effect of the gap between the rollers on the thickness of C3D^{2}G; (b) Optical image of C3D^{2}G with 15.2 μm thickness and 30% infill placed on a Kimwipe sheet. (A colour version of this figure can be viewed online.)

3.2. *Deformation mechanism and microstructure evolution due to cold rolling compression*

Compared to other forms of 3D graphene, 3D^{2}G revealed a very distinctive behavior after cold rolling with partial relaxation and no pronounced failure upon the stress release, thus leading to a higher final thickness than the expected one. In contrast, CVD-synthesized graphene foam reported in the literature is mechanically weak and requires polymer support, also breaks and shatters into pieces under minimal stress [6,10,24,34]. On the contrary, graphene aerogels are very strong and show 100% recovery after the stress is removed [3,16,35]. Understanding the changes in microstructure and the deformation mechanism can reveal the reason behind the unique behavior of 3D^{2}G under rolling compression.

The surface and the cross-section of 30% and 40% infill C3D^{2}G processed with a 155 μm rolling gap were analyzed using Scanning Electron Microscopy (SEM). As revealed in Fig. 3a and by the laser-cut cross-sectional image in Fig. 1a, the surface of 3D^{2}G looks rough with interconnected closed-pore globular morphology with graphene flakes arranged within the 3D space. After rolling compression, the surface was flattened as shown in Fig. 3b. Top-view SEM images of 30% and 40% infill 3D^{2}G taken at different magnifications, are displayed in Fig. S1 of Supplementary Information showing the stacking of 3D-printed graphene layers with cage-like structural pores. The SEM images of 30% and 40% infill C3D^{2}G are presented in Fig. 3c, d, e, and f where the rolling direction (RD) is highlighted in Fig. 3d and f. Fig. 3c and d reveal deformed pore walls illuminating bulk extrusion from every direction into the open structural pores. A similar phenomenon can be observed in the SEM images of 40% infill C3D^{2}G displayed in Fig. 3e and f where graphene was extruded from the bulk into the structural pores thus filling them. A zoomed-in view at one of the pores shown in Fig. 3f confirmed this observation. Further, the gradual morphology change from the pore center can be noticed in the SEM images Fig. 3d and f. These observations implied that the structural pores served as stress relief areas during the cold rolling and prevented structural failures. In addition, the extruded material did not experience as much stress as the bulk outside the pores thus retaining the original morphology.

A pulsed solid-state 532 nm laser milling system from Oxford Lasers was used to process the samples for cross-sectional SEM imaging. With an increase in compression, the respective C3D^{2}G showed an increase in resistance to laser irradiation resulting in longer cutting time, and a lot of deposition as a by-product of cutting was observed covering the cross-section as shown in Figs. S2 and S3 of Supplementary Information.

The performed X-Ray Diffraction (XRD) revealed the microstructure evolution due to cold rolling compression. Multiple nano-carbon peaks (002), (101), (100), (004), (110), and (006) were observed in the XRD spectrum of 3D^{2}G shown in Fig. 4a confirming random graphene flake alignment [36–38]. It is evident from the XRD spectra of pristine and compressed samples shown in Fig. 4a, b, and c, with an increase in compression, all the peaks except (002) and (004) disappeared indicating a pronounced texture with preferred orientation in [002] direction of the graphene flakes. The pattern shown in Fig. 4c resembles the XRD spectrum of Highly Oriented Pyrolytic Graphite (HOPG) except for the (006) peak which was not identified in the spectrum by the used JADE software.

The intensities of both the (002) and (004) peaks increased with increasing compression highlighting an increase of lateral crystallite size D due to compression. The observed increase in crystallite size could be caused by a slight elongation of the flakes due to micromotion during cold rolling compression. Further, a slight shift of the (002) peak toward lower 2θ was observed with an increase in compression indicating an increase in the graphene interlayer gap “d”. The equations used for XRD

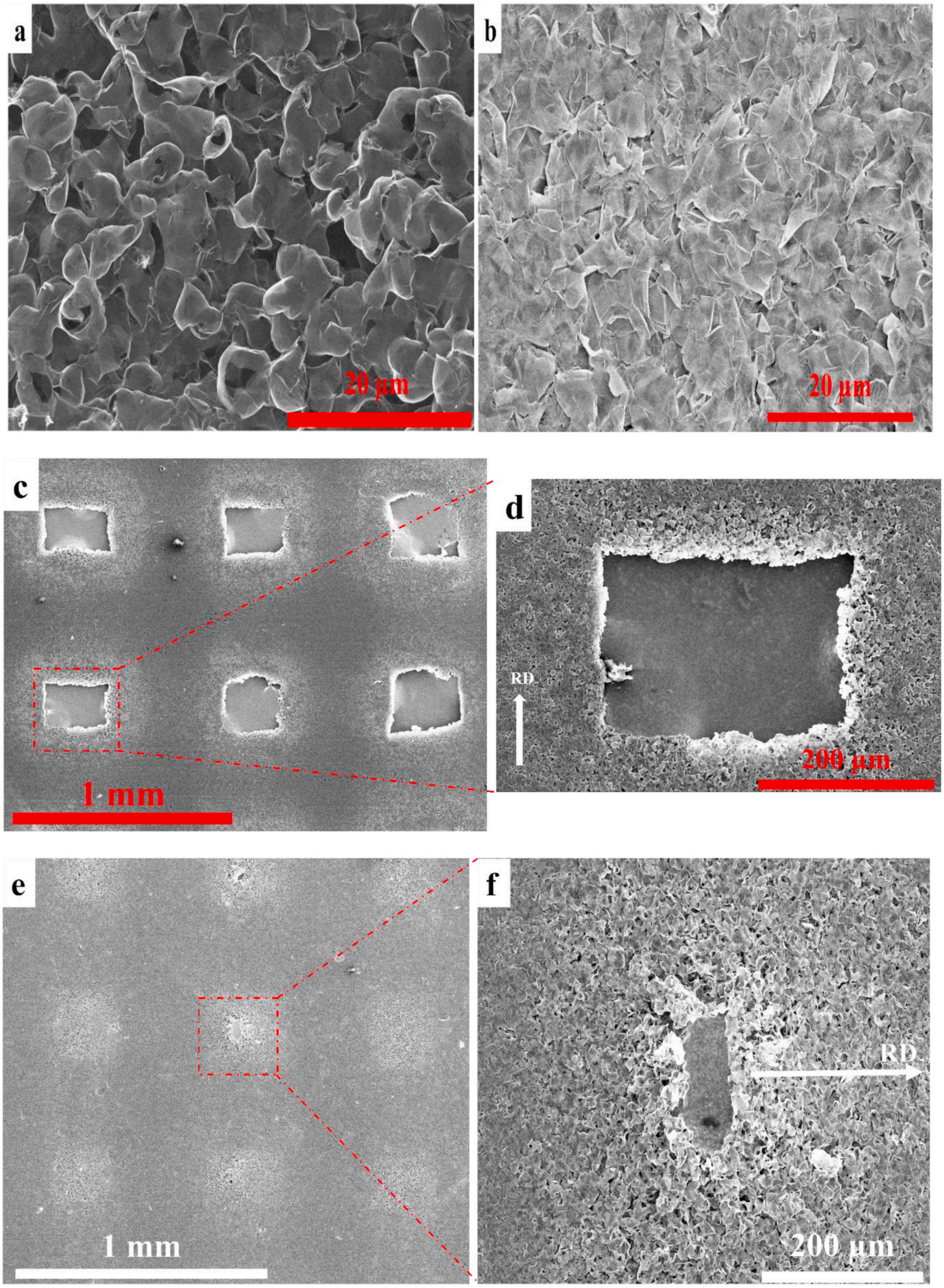

Fig. 3. SEM image of (a) $3D^2G$; (b) $C3D^2G$; (c) 30% infill $C3D^2G$; (d) Zoomed-in 30% infill $C3D^2G$; (e) 40% infill $C3D^2G$; (f) Zoomed-in 40% infill $C3D^2G$. (A colour version of this figure can be viewed online.)

calculations were presented in Supplementary Information. The shift of the 002 peak could be caused by minor delamination of graphene layers within the flakes that were subjected to folding and crimping, or due to an equipment error [39,40]. An atomic resolution TEM study is expected to clarify this observation.

Transmission Electron Microscopy (TEM) study detailed in the Supplementary Information, also Focused Ion Beam (FIB)-processed and SEM imaged $C3D^2G$ sample of 15.2 μm thickness, shown in Fig. 4d, confirmed the XRD results, suggesting folding, stacking, and alignment of graphene flakes parallel to the surface. Here, an analogy can be sought between our $3D^2G$ and a polycrystalline metal exposed to cold rolling. Seems both materials behave similarly, especially when it comes to flake/grain alignment and bulk extrusion under compression. We believe that such observation is reported for the first time in this work.

Shifting and broadening of XRD peaks due to change in the interlayer gap and structural damage of graphite, glassy carbon, mono, and few-layer graphene under stress was reported in the literature [27,41–43]. In contrast, no significant shift of the XRD peaks was observed in $C3D^2G$. The experimental results obtained from SEM, XRD, and TEM studies reveal the high cold rolling compressive stress was accommodated via bulk extrusion into the structural pores of $3D^2G$ as a macroscale deformation phenomenon preventing structural failure due to stress accumulation. At the microscale, an increase in compression, crimping, folding, stacking, and alignment of graphene flakes was evident resulting in a different microstructure and texture of $C3D^2G$ than $3D^2G$.

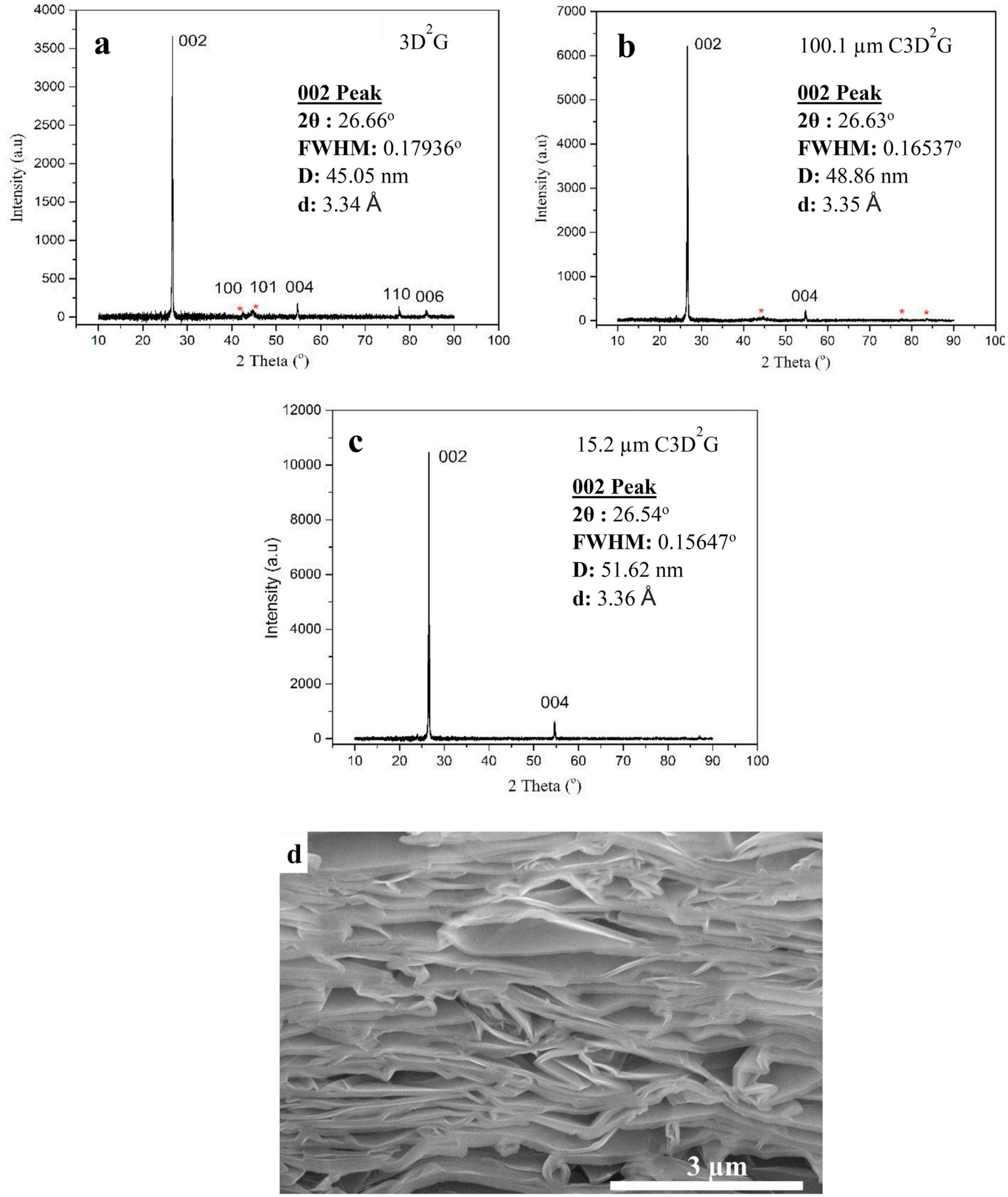

Fig. 4. XRD spectra of (a) pristine 3D^{2}G; (b) 100.1 μm thin C3D^{2}G; (c) 15.2 μm thin C3D^{2}G. D represents the lateral crystallite size and d is the interlayer gap between the graphene layers; (d) Cross-sectional SEM image of 15.2 μm thick C3D^{2}G cut by FIB perpendicular to the RD. (A colour version of this figure can be viewed online.)

3.3. Raman mapping of C3D^{2}G

The performed complex material characterization revealed the deformation mechanism at micro and macro scales. For better understanding of the compression effect on the flake's behavior in the bulk, along with the type of the experienced stress (compression or tensile), a detailed 2D Raman study was conducted.

With abilities to track stress, strain, defects, doping, stacking faults, the number of layers, etc., via peaks positions, intensity, shape, area, and Full Width at Half Maximum (FWHM) in a very precise volume, Raman Spectroscopy proved to be a very powerful technique. Raman spectral maps at 50× magnification over a 100 μm × 100 μm area were acquired with 10,201 spectral points in each map from 3D^{2}G and C3D^{2}G. Intensity ratio I(G)/I(2D), 2D peak FWHM, and G peak position maps of pristine 3D^{2}G and 15.2 μm thick C3D^{2}G are shown in Fig. S6 of Supplementary Information. A better representation of the data from these maps was shown as histograms plotted in Figs. 5 and 6.

The graphene Raman G peak is very sensitive to strain and shifts toward higher or lower Raman shift values thus distinguishing between the applied compressive and tensile strain. The G peak position data extracted from the G peak position maps of 3D^{2}G and C3D^{2}G is shown in Fig. 5. G Peak position of a majority of the Raman spectra recorded on 3D^{2}G are concentrated in one region where the Raman G peak position data was dispersed for C3D^{2}G. This highlights that a majority of spots on the C3D^{2}G underwent compressive strain, whereas a tensile strain was evident in only a few spots [25,26,44,45].

Further, the I(G)/I(2D) data of pristine 3D^{2}G shown in Fig. 6a is very symmetric and represents a uniform intensity distribution, while the I(G)/I(2D) data of C3D^{2}G shifted to higher intensities representing a left-skewed distribution. A similar trend can be observed in the histograms plotted from the 2D peak FWHM map data of pristine 3D^{2}G and C3D^{2}G in Fig. 6b. There, FWHM of 70 cm^{-1}+ dominates the distribution for C3D^{2}G and the 39 cm^{-1} – 70 cm^{-1} region overshadows the distribution for 3D^{2}G. Graphite or HOPG-like Raman peaks with high-intensity ratios along with shorter and wider 2D peaks were observed in the C3D^{2}G spectrum.

2D peak fitting with Voigt function (convolution of Gaussian and Lorentzian functions) along with the R^2 (coefficient of determination) is a powerful tool to track irregularity in layer stacking and differences in layer arrangement. A detailed Raman 2D peak fit analysis presented in our previous publication highlight 3D^{2}G consisting of graphene flakes with stacking faults (rotated graphene layers) that differentiate it from graphite and HOPG with Bernal stacked graphene layers [7].

A similar study was performed on C3D^{2}G. Three randomly selected spots representing different intensity ratios in Fig. S6d of Supplementary Information were chosen and the respective 2D peaks were analyzed using Voigt peak fit. The obtained results are illustrated in Fig. S7 of Supplementary Information. These maps highlight that the 2D peaks are deformed with Adj. R^2 values lower than 0.99 which is a deviation from the 2D peak of pristine 3D^{2}G with Adj. R^2 values were found to be greater than 0.99 [7], [46]. No difference in the 2D peak fit was observed at higher magnification (100×) as shown in Fig. S8 of Supplementary Information. A different 100 μm × 100 μm area was imaged at 50× (shown in Fig. S9 of Supplementary Information) and the same fit procedure was repeated. Similar observations were made where lower Adj. R^2 values were observed.

This study highlights that either compression caused a change in the graphene layer stacking towards a graphite-like arrangement, or the layer stacking was damaged due to the induced strain. In this case, graphitization may not be possible considering the mild post-processing conditions in terms of temperature and pressure. It can be speculated that delamination of the graphene flakes as seen in Fig. 4d and from the XRD data, could be the reason behind a change in the graphene layer stacking, thus resulting in spectra with deformed 2D peaks.

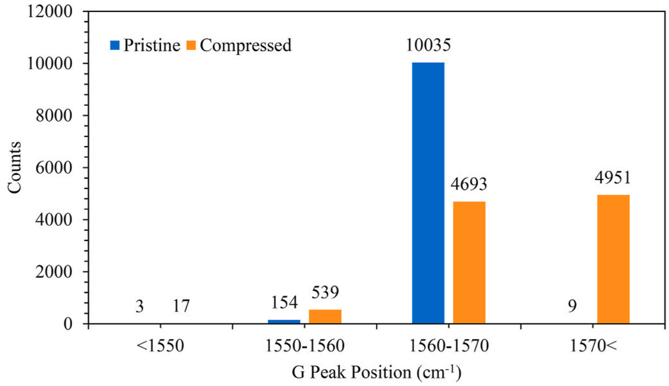

Fig. 5. G peak position bar chart for 3D^{2}G and C3D^{2}G. The data was extracted from the maps shown in Figs. S6a and b of Supplementary Information. (A colour version of this figure can be viewed online.)

4. Electrical and electrochemical property change due to cold rolling

4.1. Electrical properties

Advanced applications like energy storage, electrical conductivity, surface area, and capacitance are crucial. Fig. 7a illustrates the effect of compression on the electrical conductivity of 30% infill 3D^{2}G. The data there show an increase in the electrical conductivity from 9 S/cm for pristine 3D^{2}G to 670 S/cm for 15.2 μm thick C3D^{2}G. When changing the infill to 40% the conductivity reached the highest value of 961 S/cm, while the one for pristine 3D^{2}G with the same infill was only 17.66 S/cm, as shown in Fig. 7b. As mentioned in our previous publication, 40% infill 3D^{2}G exhibits higher electrical conductivity than 30% infill 3D^{2}G due to more mass and smaller structural pores due to higher infill [7]. In addition, the diminished porosity and lateral flake alignment caused by cold rolling would create new bridges (interfaces) between the graphene flakes which may not exist in pristine 3D^{2}G. This can increase the mean free path of the electrons thus raising the electrical conductivity. Further, in the case of C3D^{2}G with 40% infill, the infused graphene structural pores via bulk extrusion will also contribute to the higher electrical conductivity of the cold-rolled material due to improved charge transfer.

4.2. Electrochemical properties

Cyclic Voltammetry (CV) and Electrochemical Impedance Spectroscopy (EIS) were used here to analyze the electrochemical performance of C3D^{2}G. The CV curves of pristine and cold rolled samples, measured at 500 mV/s scan rate, are shown in Fig. 8a. These results highlight only a slight decrease in the capacitance for the compressed samples compared to pristine. This could be related to a reduction in the surface area, ion mobility, and ion penetration, which is directly linked to the pore size. To prove such an assumption, the surface area of the tested samples along with the available porosity have been evaluated. The specific surface area of pristine and compressed samples measured via DVS showed values of 29.637 m^2/g and 14.681 m^2/g respectively. The related adsorption-desorption plots with slight hysteresis are displayed in Figs. S10 and S11 of Supplementary Information. These measurements proved the existence of porosity (<1 μm) in all tested samples which allows diffusion of ions from the electrolyte to the bulk of the electrode. The high electrical conductivity of compressed samples would have balanced the effect of lower surface area on capacitance. As described in the literature, the greater electrical conductivity of the electrode enhances the charge transfer in carbon-based electric double-layer capacitors (EDLC) [47–51].

The results of the EIS study conducted over a frequency range of 10^5 to 10^{-2} Hz at an amplitude of 10 mV is shown in Fig. S12a where the

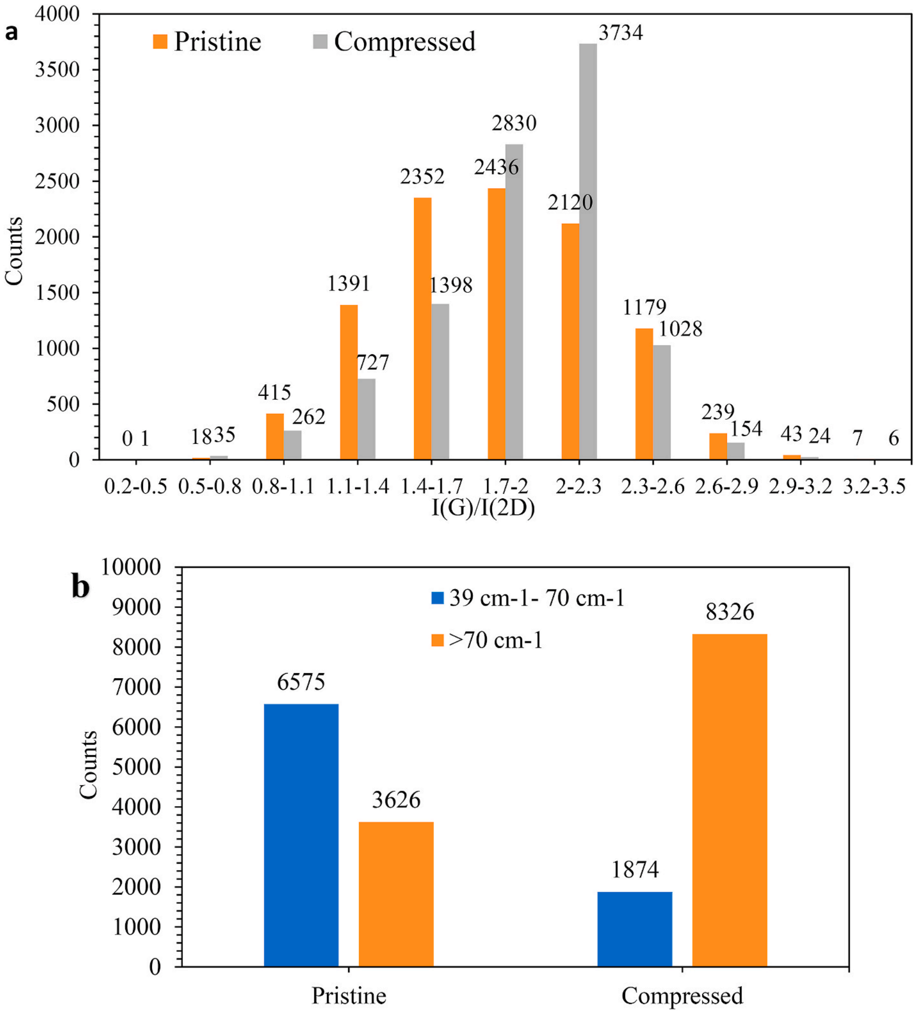

Fig. 6. (a) Histogram comparing intensity ratio of 3D^{2}G and C3D^{2}G; (b) Histogram comparing 2D peak FWHM of 3D^{2}G and C3D^{2}G obtained at 39 cm^{-1} – 70 cm^{-1} and 70+ cm^{-1} regions. (A colour version of this figure can be viewed online.)

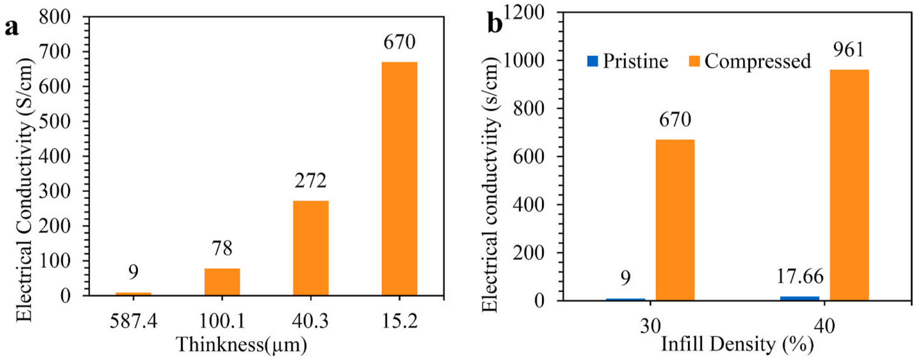

Fig. 7. (a) Electrical conductivity of 30% infill C3D^{2}G sample at various thicknesses; (b) Electrical conductivity comparison of pristine and 15.2 μm thick 30% and 40% infill C3D^{2}G samples. (A colour version of this figure can be viewed online.)

difference in the behavior of the tested samples can be observed. The equivalent circuit is displayed in the inset. Fig. S12b presents similar data obtained in the higher frequency region with an unnoticeable semicircle suggesting a low charge transfer resistance (R_{ct}) of less than 1Ω. Furthermore, the difference in the slopes of the non-vertical lines at intermediate frequencies can be observed in Fig. 8b due to non-uniform ion transport and ion path distribution to the electrode bulk, in connection with the non-uniform electrode pore size. With an increase in compression, the slope decreased where pristine 3D^{2}G exhibited a higher slope followed by 40.3 μm C3D^{2}G and 15.2 μm thick C3D^{2}G. Pristine 3D^{2}G demonstrated a superior EDL behavior compared to the cold-rolled C3D^{2}G samples due to better ion diffusion [52,53]. This behavior was expected since the compressed graphene samples exhibited decreased surface area and smaller pores after cold rolling.

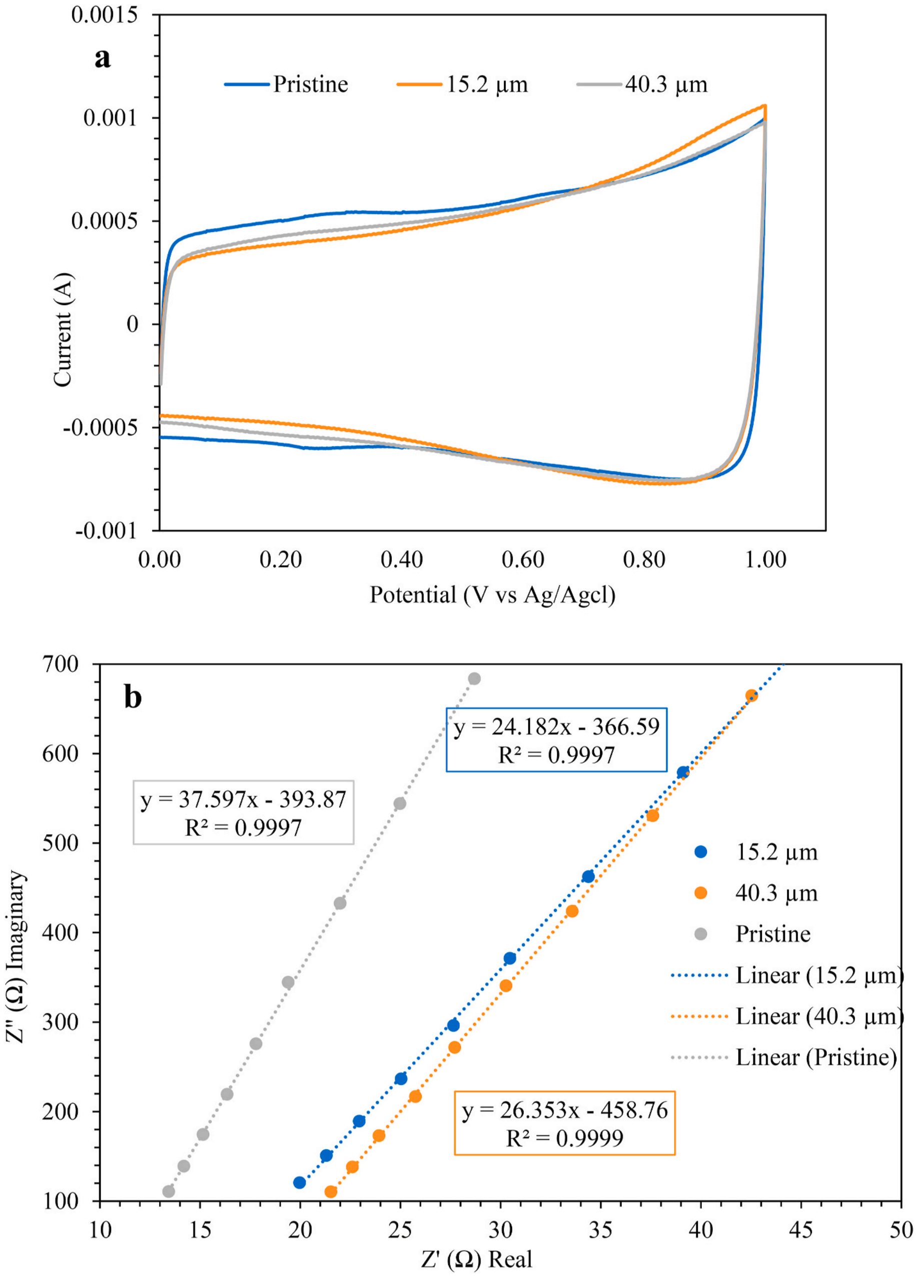

Fig. 8. (a) CV curves of pristine 3D^{2}G and C3D^{2}G with a thickness of 40.3 µm and 15.2 µm obtained at 500 mV/s scan rate; (b) Nyquist plot of 3D^{2}G and C3D^{2}G with a thickness of 40.3 µm and 15.2 µm obtained at intermediate frequencies presented with linear fits. (A colour version of this figure can be viewed online.)

5. Applications of cold rolling compression and C3D^{2}G

5.1. *Welding of 3D^{2}G using cold rolling compression*

Various welding and joining techniques were explored to overcome the limitations faced in graphene production scale-up. These techniques involve using localized thermal treatment to form bonds between defective graphene structures [54–59]. In contrast, based on the extrusion of 3D^{2}G under stress, illustrated in Fig. 3c, d, e, f, the possibility to weld different pieces via cold rolling compression at room temperature was explored. This approach offers an opportunity to make graphene samples with large areas and dimensions by joining multiple smaller pieces. The schematic shown in Fig. 9a demonstrates the procedure for welding where two 3D^{2}G pieces partly overlapping each other at the edges resulting in their welding within the overlapped area. Here, the welded samples are named W3D^{2}G. The described welding was possible due to the extrusion of graphene from one 3D^{2}G piece into the other. Fig. 9b and c shows optical images of welded two and multiple pieces of 3D^{2}G by cold rolling. In Fig. 9b the welded interface between the two pieces can be seen due to a difference in the contrast between the compressed and the welded region. Fig. 9c displays 10 different 3D^{2}G pieces joined together with random individual orientations and with multiple interfaces. Further, the welded interface between the two pieces showed a higher thickness of 15.65 µm whereas the thickness of the individual C3D^{2}G pieces was about 6.35 µm thick. The higher thickness of the weld region is due to high resistance towards compression due to more material.

5.2. *Properties of W3D^{2}G*

The electrical conductivity measurements of the welded samples were performed to understand the type of bonding within the welded

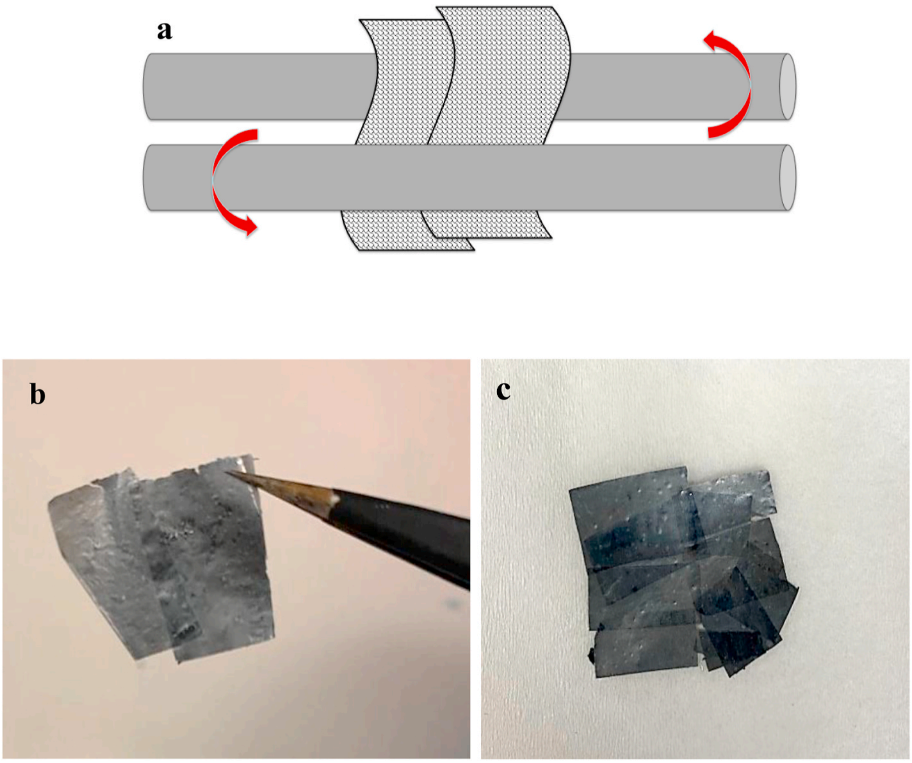

Fig. 9. (a) Schematic showing compressive welding of two $3D^2G$ pieces; (b) Optical image of $W3D^2G$ consisted of two different $3D^2G$ pieces joined together; (c) Optical image of $W3D^2G$ consisted of ten different $3D^2G$ pieces joined together. (A colour version of this figure can be viewed online.)

region. Three different samples with similar dimensions, $C3D^2G$ (not welded), and $W3D^2G$ having 0.5 cm and 1 cm welded overlap areas, were studied where their electrical conductivity normalized by weight was compared in Fig. 10a. The welded samples exhibited lower electrical conductivity due to their higher resistance compared to the sample with the no-welding region. A decrease in electrical conductivity with increased welded overlap area suggests that the bond within the welded region is not chemical, but rather a mechanical one achieved via the extrusion of graphene.

Further, the strength of the welded joint was studied using $W3D^2G$ samples with 0.5 cm and 1 cm overlap area and compared with the strength of $C3D^2G$ and $3D^2G$ having dimensions of 5 mm × 44 mm. The related experiments have been conducted using a tensile testing instrument Instron 5940, and the respective stress-strain curve for $3D^2G$ is shown in Fig. 10b. It was observed that irrespective of the welded area size, the samples always failed on spots outside the welded region as shown in Fig. S13a of Supplementary Information**.** This highlights the higher strength of the joint which exceeded that of the $C3D^2G$ itself. Despite the non-chemical nature of the bond in the welded area, the joint appeared to be very strong. This data supports the notion of successful scalability via cold rolling welding for fabricating $3D^2G$ samples with large areas and increased dimensions.

The stress-strain curves displayed in Fig. 10b show improved mechanical properties of $C3D^2G$/$W3D^2G$ when compared to just pristine $3D^2G$. The tensile strength of $C3D^2G$ and $W3D^2G$ was around 19.5 MPa whereas for $3D^2G$ it was only 0.75 MPa. FIB processed cross section imaged by SEM throughout the welded area, shown in Figs. S13b and c of Supplementary Information, reveal a uniform and seamless microstructure across the thickness of the welded region. No interface between the two welded pieces was observed in these images thus supporting the hypothesis that graphene from one $3D^2G$ was extruded into the other piece during the cold rolling thus resulting in a new bulk material with high density and strength. Further, the failure of $3D^2G$ was instantaneous where $C3D^2G$/$W3D^2G$ show declining stress past the tensile strength point due to noticeable crack propagation. The SEM image of the cross-section at the failure location of the $W3D^2G$ sample outside the welding area is shown in Fig. S13d of Supplementary Information revealing some delamination and separation.

5.3. $C3D^2G$ as a protective material and hard mask against Reactive Ion Etching (RIE) in fluorine plasma environment

High-performance electronics require downsizing electronic components with a high aspect ratio. Hard masks should withstand the harsh plasma environment and demonstrate high selectivity over silicon (Si)/silicon dioxide (SiO_2). Metal (pure metals or metal oxide) and ceramic hard masks demonstrated very high selectivity to fluorine plasma where charge accumulation on the masks and chamber contamination by particle erosion was evident [60–63]. Alternatively, carbon materials were used as hard mask material in industrial dry etching applications due to their good etch selectivity (higher than photo resists), ease of synthesis, pattern, cleaning, and removal [64–68]. Amorphous Carbon Layer (ACL) was the prime hard mask material of choice where hydrogenated and doped ACL demonstrated improved selectivity to fluorine plasma [65,66,69–71]. Further, a recent study on etch resistance of graphene and multilayer graphene (crystalline carbon) to fluorine plasma demonstrated higher selectivity than ACL due to the high reaction barrier energy of the basal graphene when interacting with F^- radicals [72]. Further, industrial dry etch chambers involve using $Si/SiO_2/Al_2O_3$ parts that are prone to erosion, degradation, and particle contamination when exposed to fluorine plasma [60,73].

Here, we propose $C3D^2G$ to serve as a reusable hard mask for patterning Si/SiO_2 and as a protective material for various parts inside RIE chambers exposed to fluorine plasma. Defect-free, high chemical stability, ability to pattern via 3D printing and customizing bulk properties via cold rolling, high gravimetric density (0.03 g/cm^3 for 1-layer solid pristine $3D^2G$ to 1.12 g/cm^3 for 6.35 μm thick $C3D^2G$ close to the density of amorphous carbon (1.18 g/cm^3)) with less surface area and

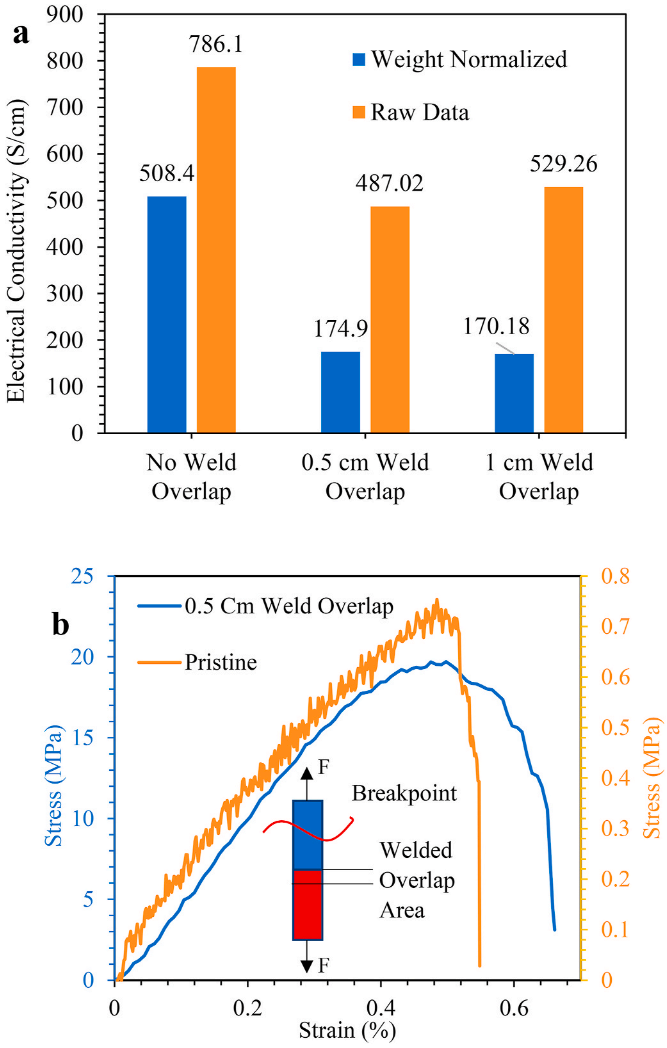

Fig. 10. (a) Effect of welding overlap on electrical conductivity normalized by weight for 2 pieces of $3D^2G$ joined together; (b) Stress-strain curve obtained by a tensile test for 2 pieces of $3D^2G$ welded together, where the welded overlap was 0.5 cm. Note that the breakpoint of the tested sample is outside the welded region. The inset there illustrates the same. (A colour version of this figure can be viewed online.)

high graphene flake alignment and production scalability are a few qualities of $C3D^2G$ that make it compete with industrial carbon hard masks. The selectivity of various carbon materials over Si/SiO_2 along with $3D^2G$ and $C3D^2G$ were summarized in Table S1 of Supplementary Information.

5.3.1. Procedure to make $C3D^2G$ Reactive Ion Etching hard mask for selective etching and surface protection

$3D^2G$ was synthesized as described in detail in our previous publication [7]. In addition, the procedure was summarized in Section 2.1 of this manuscript. The synthesized $3D^2G$ was sandwiched between two SS shims and cold rolled to the required thickness (density). The cold rolled sandwich ($3D^2G$ between the SS shims) was dipped in an ethanol bath and the $C3D^2G$ was separated and dried using Kim wipes. The dried $C3D^2G$ was placed and aligned on a polycrystalline silicon sample with native oxide or silicon wafer with a thick SiO_2 layer where a few drops of ethanol were added to the $C3D^2G$ mask and dried. This allowed the $C3D^2G$ mask to adhere strongly after complete evaporation of ethanol due to capillary forces. Samples with the $C3D^2G$ mask were etched using RIE. The $C3D^2G$ mask was removed by the addition of ethanol thus lifting the mask after etching without any damage, thus preparing it for reuse.

5.3.2. RIE protective material

Solid 1-layer $C3D^2G$ with a thickness of 6.35 μm was studied as a protective material against reactive plasma etching. For both hard mask and protective material applications, etch resistance to fluorine plasma plays a crucial role. Etch rates of polycrystalline silicon, $C3D^2G$, $3D^2G$, and 99.9% pure graphite with a calculated gravimetric density of ~1.7 g/cm^3, have been experimentally studied. Four samples of each, $C3D^2G$ and 1-layer solid $3D^2G$, were placed on two different glass slides. A few drops of ethanol were added on top of the samples. The samples adhered strongly to the glass slides after complete evaporation of ethanol due to the capillary effect, which was tested by blowing pressurized air at the interface.

Polycrystalline silicon with native oxide and graphite was mounted as control samples on another glass slide using double-sided Kapton tape. All the glass slides with the mounted samples on them were exposed to etching simultaneously using 30 sccm CF_4 and 2 sccm Ar plasma at 200 mTorr. For these experiments, a Nordson March CS-1701 RIE reactor was employed using different etching power for 2 or 4 min. After conducting the dry etching, a few drops of ethanol were added to the samples to promote separating the etched $C3D^2G$ from the glass slides. The etch rates were evaluated by tracking the sample weights before and after etching and the obtained values were normalized by area, i.e., $mg.s^{-1}.mm^{-2}$. The conducted experiments were designed to understand the effects of plasma power and etching time on the etch rate of the tested samples. The etch data and related etch rates for all the samples at different process parameters are presented in Table 1.

The obtained data revealed a lower etch rate of $C3D^2G$ when compared to $3D^2G$, graphite, and polycrystalline silicon under all employed etch parameters. At 100W power and etch time of 2 min, the etch rates of $3D^2G$, graphite, and silicon were 1.57, 2.95, and 29.8 times the etch rate of $C3D^2G$ respectively. The lower etch rate of $C3D^2G$ over $3D^2G$ can be attributed to the lower porosity observed on the surface and in the bulk of this material. The exposed to etching large internal surface area of the graphene pore walls was the major reason for the high etch rate of $3D^2G$. On the other hand, both $C3D^2G$ and $3D^2G$ performed better than graphite. The presence of defects on the basal plane (surface and edge), and surface damage (pits and surface finish due to manufacturing) would have resulted in a lower etch resistance of graphite compared to CVD-synthesized graphene such as $3D^2G$ and $C3D^2G$.

When the dry etching was performed at a higher power level of 300 W, the results changed slightly compared to the case of 100 W. The etch rates of $3D^2G$, graphite, and silicon were 1.78, 1.4, and 13 times the etch rate of $C3D^2G$ respectively. With the increase in power, the etch rate of $C3D^2G$ and $3D^2G$ increased by 10.36 and 11.8 times. In contrast, the etch rate of graphite and silicon increased by ~5 times. This greater increase in etches rate of $C3D^2G$ can be related to the enhanced generation of more energetic radicals at higher plasma power resulting in greater diffusion of the plasma species into the bulk through the surface pores, and also due to enhanced etching of staked graphene flakes thus opening access to the pores in the bulk. With an increase in etching time, no change in the etch rate was observed. Here, the removal of material at a consistent rate with time was noticed confirming that $C3D^2G$ and $3D^2G$ are uniform in structure and properties like silicon and graphite.

Etch rates in fluorine plasma of various carbon-based mask materials compared with $C3D^2G$, showing etch selectivity towards Si/SiO_2, are displayed in Table S1 of Supplementary Information. This table revealed the very good performance of our $C3D^2G$ compared to the listed materials there.

5.3.3. Reusable hard mask

For this application $C3D^2G$ with 30% infill and a thickness of 15.2 μm was used. As reported earlier, the much lower etch rate of $C3D^2G$ compared to polycrystalline silicon along with the ability to be

Table 1

Etch rate of C3D^{2}G, 3D^{2}G, graphite, and silicon was obtained at different plasma power and etch times. The etch rate values have been normalized by the processing time (Total Etch), or by both processing time and sample area (Etch Rate).

Plasma Power	300W				100W	
Material	Etch Rate (mg.s^{-1}.mm^{-2})		Total Etch (mg.mm^{-2})		Etch Rate (mg.s^{-1}.mm^{-2})	Total Etch (mg.mm^{-2})
	2mins	4mins	2mins	4mins	2 min	
C3D^{2}G	2.40040E-06	2.50371E-06	2.88048E-04	6.00890E-04	2.31666E-07	2.78000E-05
3D^{2}G	4.29086E-06	4.22168E-06	5.04854E-04	1.01320E-03	3.64533E-07	4.37439E-05
Graphite	3.38061E-06	3.49040E-06	4.05673E-04	8.37697E-04	6.84393E-07	8.21271E-05
Polycrystalline Silicon	3.13710E-05	3.07782E-05	3.76452E-03	7.38676E-03	6.91024E-06	8.29228E-04

patterned makes this material a good contender for hard masks in RIE. 3D^{2}G with a rectilinear pattern of various sizes was converted to C3D^{2}G and adhered to single crystal silicon wafers having orientation (110) and coated with 300 μm thermal oxide. The prepared wafers with C3D^{2}G masks on top were etched using a 100W RIE process. The plasma environment included 30 sccm of CF_4 and 2 sccm of argon at a total pressure of 200 mTorr. Fig. 11a, b, and c display optical images of the silicon wafer with the mask before etching, after etching, and after the removal of the mask respectively. A clear change in the contrast of the wafer between the plasma-exposed and unexposed areas of the wafer can be seen in Fig. 11c.

The patterns etched for 1, 2, and 3 min were studied using a stylus profilometer, and the obtained depth profiles of the created trenches are shown in Fig. S14 of Supplementary Information. With increasing the etch time, the depth of the etched pattern increased. The wafer surface outside the trenches looks smooth highlighting no under-etching thanks to the good adhesion between the mask and the wafer. Also, the walls of the trenches appear straight and vertical suggesting anisotropic etching.

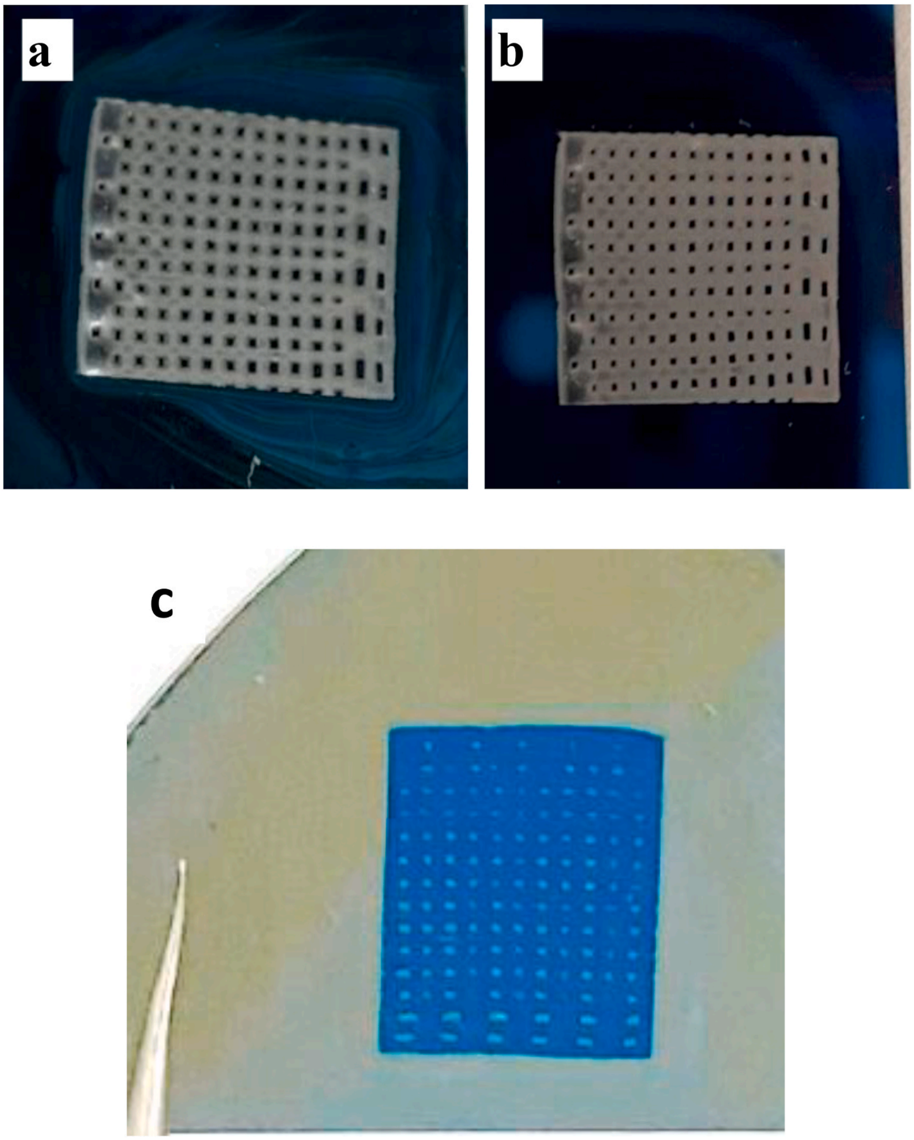

Fig. 11. Optical images of the wafer with C3D^{2}G mask: (a) Before RIE; (b) After RIE; (c) After removal of the mask; The used plasma power in these experiments was 100W, and the plasma gas composition consisted of 30 sccm CF_4 and 2 sccm argon. (A colour version of this figure can be viewed online.)

After the conducted RIE, the mask was lifted off from the wafer intact using ethanol, dried, and stored for future reuse.

6. Conclusion

It has been reported here successful employment of cold rolling as a post-processing technique to improve the properties of $3D^2G$, along with a detailed characterization of this material after such a treatment. The XRD, SEM, and TEM data suggested forced alignment and stacking of the graphene flakes due to cold rolling. Though cold rolling decreased the surface area and pore size, this procedure succeeded in achieving great electrical conductivity, higher tensile strength, and high resistance to laser irradiation. Further, the observed extrusion behavior and filling of structural pores when compressing $3D^2G$ were found to be the reason for lacking stress accumulation and failure after cold rolling. This quality allowed welding together multiple $3D^2G$ pieces. The achieved joining was mechanical; however, it provided a strong bonding between the welded pieces and offered an alternative to produce large graphene pieces. Due to the high density and flake alignment, $C3D^2G$ demonstrated high RIE resistance over Si, SiO_2, and graphite in a fluorine plasma environment and was successfully tested as a plasma protective material, including as a hard mask for semiconductor processing. Based on the experimental data, the obtained architecture of $3D^2G$ after cold rolling suggested a new bulk morphology of the compressed material which significantly enhanced its properties. Thus, we believe that the described here efforts provided valuable information about the relationship between microstructure, properties, and applications of $C3D^2G$.

CRediT authorship contribution statement

Vamsi Krishna Reddy Kondapalli: Conceptualization, Methodology, Formal analysis, Investigation, Validation, Visualization, Data curation, and, Writing – original draft. **Guangqi Zhang:** Methodology, and, Investigation. **Yu Zhang:** Investigation. **Mahnoosh Khosravifar:** Investigation. **Kyle Brittingham:** Conceptualization, and, Methodology. **Nhat Phan:** Investigation. **Sergey Yarmolenko:** Investigation, Formal analysis, and, Validation. **Je- Hyeong Bahk:** Investigation. **Vesselin Shanov:** Conceptualization, Methodology, Resources, Writing – review & editing, Supervision, Project administration, and, Funding acquisition.

Declaration of competing interest

The authors declare that they have no known competing financial interests or personal relationships that could have appeared to influence the work reported in this paper.

Acknowledgments

This research study was partially supported by the National Institute for Occupational Safety and Health through a grant #T42OH008432from the Pilot Research Project Training Program of the University of Cincinnati (UC) Education and Research Center. The authors also acknowledge the financial support from NASA [grant 80NSSC21P2821], NSF [grants IIP-2016484 and CBET-2028625], and the UC Collaborative Research Advancement grant #1018371. One of the authors (V.K.R.K) would like to thank the Graduate Student Government (GSG) at UC for the Research Fellowship and the Department of Engineering Education at UC for the provided financial support via a Graduate Assistantship. The authors would like to acknowledge the help of Dr. Melodie Fickenscher at the UC Advanced Materials Characterization Center and Ronald Flenniken and Jeffery Simkins at the UC Clean Room. The authors would like to thank Daniel Burnett, Armando Garcia, and Chris Vander Tuuk from Surface Measurements Systems for the specific surface area measurements using their DVS instruments.

Appendix A. Supplementary data

Supplementary data to this article can be found online at https://doi.org/10.1016/j.carbon.2023.03.004.

References

[1] Z. Sun, S. Fang, Y.H. Hu, 3D graphene materials: from understanding to design and synthesis control, Chem. Rev. (2020) 120 10336–10453, https://doi.org/10.1021/acs.chemrev.0c00083.

[2] S. Chandrasekaran, M.R. Cerón, M.A. Worsley, CHAPTER 1 Engineering the Architecture of 3D Graphene-Based Macrostructures, 2021, pp. 1–40, https://doi.org/10.1039/9781839162480-00001.

[3] Q. Zhang, F. Zhang, S.P. Medarametla, H. Li, C. Zhou, D. Lin, 3D printing of graphene aerogels, Small 12 (2016) 1702–1708, https://doi.org/10.1002/smll.201503524.

[4] Y. Xu, K. Sheng, C. Li, G. Shi, Self-assembled graphene hydrogel via a one-step hydrothermal process, ACS Nano 4 (2010) 4324–4330, https://doi.org/10.1021/nn101187z.

[5] Z.J. Li, B.C. Yang, S.R. Zhang, C.M. Zhao, Graphene oxide with improved electrical conductivity for supercapacitor electrodes, Appl. Surf. Sci. 258 (2012) 3726–3731, https://doi.org/10.1016/j.apsusc.2011.12.015.

[6] A.E. Jakus, E.B. Secor, A.L. Rutz, S.W. Jordan, M.C. Hersam, R.N. Shah, Three-dimensional printing of high-content graphene scaffolds for electronic and biomedical applications, ACS Nano 9 (2015) 4636–4648, https://doi.org/10.1021/acsnano.5b01179.

[7] V.K.R. Kondapalli, X. He, M. Khosravifar, S. Khodabaksh, B. Collins, S. Yarmolenko, et al., CVD synthesis of 3D-Shaped 3D graphene using a 3D-printed nickel–PLGA catalyst precursor, ACS Omega 6 (2021) 29009–29021, https://doi.org/10.1021/acsomega.1c04072.

[8] D. DeArmond, L. Zhang, R. Malik, K.V.K. Reddy, N.T. Alvarez, M.R. Haase, et al., Scalable CVD synthesis of three-dimensional graphene from cast catalyst, Mater. Sci. Eng. B 254 (2020), 114510, https://doi.org/10.1016/j.mseb.2020.114510.

[9] L. Zhang, D. DeArmond, N.T. Alvarez, D. Zhao, T. Wang, G. Hou, et al., Beyond graphene foam, a new form of three-dimensional graphene for supercapacitor electrodes, J. Mater. Chem. 4 (2016) 1876–1886, https://doi.org/10.1039/C5TA10031C.

[10] F. Yavari, Z. Chen, A.V. Thomas, W. Ren, H.M. Cheng, N. Koratkar, High sensitivity gas detection using a macroscopic three-dimensional graphene foam network, Sci. Rep. 1 (2011) 1–5, https://doi.org/10.1038/srep00166.

[11] G. Chen, Y. Liu, F. Liu, X. Zhang, Fabrication of three-dimensional graphene foam with high electrical conductivity and large adsorption capability, Appl. Surf. Sci. 311 (2014) 808–815, https://doi.org/10.1016/j.apsusc.2014.05.171.

[12] X. Cao, Y. Shi, W. Shi, G. Lu, X. Huamg, Q. Yan, et al., Preparation of novel 3D graphene networks for supercapacitor applications, Small 7 (2011) 3163–3168, https://doi.org/10.1002/smll.201100990.

[13] C. Hu, D. Liu, Y. Xiao, L. Dai, Functionalization of graphene materials by heteroatom-doping for energy conversion and storage, Prog. Nat. Sci. Mater. Int. 28 (2018) 121–132, https://doi.org/10.1016/j.pnsc.2018.02.001.

[14] N. Talukder, Y. Wang, B.B. Nunna, E.S. Lee, Nitrogen-doped graphene nanomaterials for electrochemical catalysis/reactions: a review on chemical structures and stability, Carbon N. Y. 185 (2021) 198–214, https://doi.org/10.1016/j.carbon.2021.09.025.

[15] F. Novotný, V. Urbanová, J. Plutnar, M. Pumera, Preserving fine structure details and dramatically enhancing electron transfer rates in graphene 3D-printed electrodes via thermal annealing: toward nitroaromatic explosives sensing, ACS Appl. Mater. Interfaces 11 (2019) 35371–35375, https://doi.org/10.1021/acsami.9b06683.

[16] W. Tang, L. Peng, C. Yuan, J. Wang, S. Mo, C. Zhao, et al., Facile synthesis of 3D reduced graphene oxide and its polyaniline composite for super capacitor application, Synth. Met. 202 (2015) 140–146, https://doi.org/10.1016/j.synthmet.2015.01.031.

[17] R. Yadav, C.K. Dixit, Synthesis, characterization and prospective applications of nitrogen-doped graphene: a short review, J. Sci. Adv. Mater. Devices 2 (2017) 141–149, https://doi.org/10.1016/j.jsamd.2017.05.007.

[18] L. Zhang, D. DeArmond, N.T. Alvarez, R. Malik, N. Oslin, C. McConnell, et al., Flexible micro-supercapacitor based on graphene with 3D structure, Small 13 (2017), 1603114, https://doi.org/10.1002/smll.201603114.

[19] Y. Fang, Y.Y. Hsieh, M. Khosravifar, K. Johnson, P.K. Adusei, S.N. Kanakaraj, et al., Lithiophilic current collector based on nitrogen doped carbon nanotubes and three-dimensional graphene for long-life lithium metal batteries, Mater. Sci. Eng. B 267 (2021), 115067, https://doi.org/10.1016/j.mseb.2021.115067.

[20] K.M. Joseph, V. Shanov, Symmetric supercapacitor based on nitrogen-doped and plasma-functionalized 3D graphene, Batteries 8 (2022) 258, https://doi.org/10.3390/batteries8120258.

[21] Z. Luo, X. Hu, X. Tian, C. Luo, H. Xu, Q. Li, et al., Structure-property relationships in graphene-based strain and pressure sensors for potential artificial intelligence applications, Sensors 19 (2019), https://doi.org/10.3390/s19051250.

[22] H. Huang, S. Su, N. Wu, H. Wan, S. Wan, H. Bi, et al., Graphene-based sensors for human health monitoring, Front. Chem. 7 (2019) 399, https://doi.org/10.3389/fchem.2019.00399.

[23] M. Cao, J. Su, S. Fan, H. Qiu, D. Su, L. Li, Wearable piezoresistive pressure sensors based on 3D graphene, Chem. Eng. J. 406 (2021), 126777, https://doi.org/10.1016/j.cej.2020.126777.

[24] T. Du, Z. Xiong, L. Delgado, W. Liao, J. Peoples, R. Kantharaj, et al., Wide range continuously tunable and fast thermal switching based on compressible graphene composite foams, Nat. Commun. 121 (12) (2021) 1–10, https://doi.org/10.1038/s41467-021-25083-8, 2021.

[25] C. Si, Z. Sun, F. Liu, Strain engineering of graphene: a review, Nanoscale 8 (2016) 3207–3217, https://doi.org/10.1039/C5NR07755A.

[26] Y. Wang, J.E. Panzik, B. Kiefer, K.K.M. Lee, Crystal structure of graphite under room-temperature compression and decompression, Sci. Rep. 2 (2012) 1–7, 10.1038%2Fsrep.00520.

[27] S.M. Clark, K.J. Jeon, J.Y. Chen, C.S. Yoo, Few-layer graphene under high pressure: Raman and X-ray diffraction studies, Solid State Commun. 154 (2013) 15–18, https://doi.org/10.1016/j.ssc.2012.10.002.

[28] C. Androulidakis, E.N. Koukoras, John Parthenious, G. Kalosakas, K. papagelis, C. Galiotis, et al., Graphene flakes under controlled biaxial deformation, Sci. Rep. 51 (5) (2015) 1–11, https://doi.org/10.1038/srep18219, 2015.

[29] C. Wang, C. Zhang, S. Chen, The microscopic deformation mechanism of 3D graphene foam materials under uniaxial compression, Carbon N. Y. 109 (2016) 666–672, https://doi.org/10.1016/j.carbon.2016.08.084.

[30] A. Nieto, B. Boesl, A. Agarwal, Multi-scale intrinsic deformation mechanisms of 3D graphene foam, Carbon N. Y. 85 (2015) 299–308, https://doi.org/10.1016/j.carbon.2015.01.003.

[31] D. Pan, C. Wang, T.C. Wang, Y. Yao, Graphene foam: uniaxial tension behavior and fracture mode based on a mesoscopic model, ACS Nano 11 (2017) 8988–8997, https://doi.org/10.1021/acsnano.7b03474.

[32] C. Wang, D. Pan, S. Chen, Energy dissipative mechanism of graphene foam materials, Carbon N. Y. 132 (2018) 641–650, https://doi.org/10.1016/j.carbon.2018.02.085.

[33] C. Wang, C. Zhang, S. Chen, Micro-mechanism and influencing factors of graphene foam elasticity, Carbon N. Y. 148 (2019) 267–276, https://doi.org/10.1016/j.carbon.2019.03.084.

[34] Z. Chen, W. Ren, L. Gao, B. Liu, S. Pei, H.M. Cheng, Three-dimensional flexible and conductive interconnected graphene networks grown by chemical vapour deposition, Nat. Mater. *106* (10) (2011) 424–428, https://doi.org/10.1038/nmat3001, 2011.

[35] Y. Wu, N. Yi, L. Huang, T. Zhang, S. Fang, H. Chang, et al., Three-dimensionally bonded spongy graphene material with super compressive elasticity and near-zero Poisson's ratio, Nat. Commun. *61* (6) (2015) 1–9, https://doi.org/10.1038/ncomms7141, 2015.

[36] K. Kakaei, M.D. Esrafili, A. Ehsani, A. Ehsan, Graphene surfaces : particles and catalysts/Karim Kakaei, mehdi D. Esrafili, ali ehsani, Graphene surfaces Part. Catal (2019).

[37] Q. Cheng, Y. Okamoto, N. Tamura, M. Tsuji, S. Maruyama, Y. Matsuo, Graphene-like-graphite as fast-chargeable and high-capacity anode materials for lithium ion batteries, Sci. Rep. *71* (7) (2017) 1–14, https://doi.org/10.1038/s41598-017-14504-8, 2017.

[38] J. Sha, C. Gao, S.K. Lee, N. Li, N. Zhao, J.M. Tour, et al., Preparation of three-dimensional graphene foams using powder metallurgy templates, ACS Nano 10 (2016) 1411–1416, https://doi.org/10.1021/acsnano.5b06857.

[39] C. Cong, T. Yu, Enhanced ultra-low-frequency interlayer shear modes in folded graphene layers, Nat. Commun. *51* (5) (2014) 1–7, https://doi.org/10.1038/ncomms5709, 2014.

[40] P. Koskinen, Bending-induced delamination of van der Waals solids, J. Phys. Condens. Matter 25 (2013), 395303, https://doi.org/10.1088/0953-8984/25/39/395303.

[41] M.S. Seehra, V. Narang, U.K. Geddam, A.B. Stefaniak, Correlation between X-ray diffraction and Raman spectra of 16 commercial graphene–based materials and their resulting classification, Carbon N. Y. 111 (2017) 380–385, https://doi.org/10.1016/j.carbon.2016.10.010.

[42] Y. Wang, J.E. Panzik, B. Kiefer, K.K.M. Lee, Crystal structure of graphite under room-temperature compression and decompression, Sci. Rep. *21* (2) (2012) 1–7, https://doi.org/10.1038/srep00520, 2012.

[43] Y. Shibazaki, Y. Kono, G. Shen, Compressed glassy carbon maintaining graphite-like structure with linkage formation between graphene layers, Sci. Rep. *91* (9) (2019), https://doi.org/10.1038/s41598-019-43954-5, 1–18 (209.

[44] M.A. Bissett, M. Tsuji, H. Ago, Strain engineering the properties of graphene and other two-dimensional crystals, Phys. Chem. Chem. Phys. 16 (2014) 11124–11138, https://doi.org/10.1039/C3CP55443K.

[45] O. Frank, G. Tsoukleri, J. Parthenios, K. Papagelis, I. Riaz, R. Jalil, et al., Compression behavior of single-layer graphenes, ACS Nano 4 (2010) 3131–3138, https://doi.org/10.1021/nn100454w.

[46] S. Roscher, R. Hoffmann, O. Ambacher, Determination of the graphene-graphite ratio of graphene powder by Raman 2D band symmetry analysis, Anal. Methods 11 (2019) 1180–1191, https://doi.org/10.1039/C8AY02619J.

[47] H. Wang, L. Pilon, Physical interpretation of cyclic voltammetry for measuring electric double layer capacitances, Electrochim. Acta 64 (2012) 130–139, https://doi.org/10.1016/j.electacta.2011.12.118.

[48] J. Sánchez-González, F. Stoeckli, T.A. Centeno, The role of the electric conductivity of carbons in the electrochemical capacitor performance, J. Electroanal. Chem. 657 (2011) 176–180, https://doi.org/10.1016/j.jelechem.2011.03.025.

[49] A.G. Pandolfo, A.F. Hollenkamp, Carbon properties and their role in supercapacitors, J. Power Sources 157 (2006) 11–27, https://doi.org/10.1016/j.jpowsour.2006.02.065.

[50] M.D. Stoller, S. Park, Z. Yanwu, J. An, R.S. Ruoff, Graphene-Based ultracapacitors, Nano Lett. 8 (2008) 3498–3502, https://doi.org/10.1021/nl802558y.

[51] A.G. Pandolfo, G.J. Wilson, T.D. Huynh, A.F. Hollenkamp, The influence of conductive additives and inter-particle voids in carbon EDLC electrodes, Fuel Cell. 10 (2010) 856–864, https://doi.org/10.1002/fuce.201000027.

[52] B.A. Mei, O. Munteshari, J. Lau, B. Dunn, L. Pilon, Physical interpretations of nyquist plots for EDLC electrodes and devices, J. Phys. Chem. C 122 (2018) 194–206, https://doi.org/10.1021/acs.jpcc.7b10582.

[53] J. Wu, Understanding the electric double-layer structure, capacitance, and charging dynamics, Chem. Rev. 122 (2022) 10821–10859, https://doi.org/10.1021/acs.chemrev.2c00097.

[54] Y. Yao, K.K. Fu, S. Zhu, J. Dai, Y. Wang, G. Pastel, et al., Carbon welding by ultrafast joule heating, Nano Lett. 16 (2016) 7282–7289, https://doi.org/10.1021/acs.nanolett.6b03888.

[55] Y. Liu, C. Liang, A. Wei, Y. Jiang, Q. Tian, Y. Wu, et al., Solder-free electrical Joule welding of macroscopic graphene assemblies, Mater. Today Nano 3 (2018) 1–8, https://doi.org/10.1016/j.mtnano.2018.09.005.

[56] K. Keramatnejad, Y.S. Zhou, D.W. Li, R. Golgir, X. Huang, J.F. Song, et al., Reducing Graphene-Metal Contact Resistance via Laser Nano-Welding, 2017, pp. 372–377, https://doi.org/10.1117/12.2253752 10092.

[57] D. Chakravarty, C.S. Tiwary, C.F. Woellner, S. Radhakrishnan, S. Vinod, S. Ozden, et al., 3D porous graphene by low-temperature plasma welding for bone implants, Adv. Mater. 28 (2016) 8959–8967, https://doi.org/10.1002/adma.201603146.

[58] R. Zou, Z. Zhang, K. Xu, L. Jiang, Q. Tian, Y. Sun, et al., A method for joining individual graphene sheets, Carbon N. Y. 50 (2012) 4965–4972, https://doi.org/10.1016/j.carbon.2012.06.031.

[59] X. Wu, Joining of Graphene by Particle Beam Irradiation and its Properties, 2018, pp. 99–142, https://doi.org/10.1007/978-981-10-6457-9_5.

[60] W.K. Wang, Y.X. Lin, Y.J. Xu, Structural and fluorine plasma etching behavior of sputter-deposition yttrium fluoride film, Nanomater 8 (2018), https://doi.org/10.3390/nano8110936, 936 8, 936 (2018.

[61] B. Glück, The influence of etching conditions on surface contamination during silicon etching in CF4 plasma, Cryst. Res. Technol. 25 (1990) 813–818, https://doi.org/10.1002/crat.2170250714.

[62] G.F. Ding, H.P. Mao, Y.L. Cai, Y.H. Zhang, X. Yao, X.L. Zhao, et al., Micromachining of CVD diamond by RIE for MEMS applications, Diam. Relat. Mater. 14 (2005) 1543–1548, https://doi.org/10.1016/j.diamond.2005.04.011.

[63] L. Chen, X. Wang, Y. Wei, C. Zhou, A magnetic metal hard mask on silicon substrate for direct patterning ultra-high-resolution OLED displays, Micromachines 13 (2022), https://doi.org/10.3390/mi13070997, 997 13, 997 (2022.

[64] M. Massi, R.D. Mansano, H.S. Maciel, C. Otani, P. Verdonck, L.N.B.M. Nishioka, et al., Effects of plasma etching on DLC films, Thin Solid Films 343–344 (1999) 381–384, https://doi.org/10.1016/S0040-6090(98)01691-5.

[65] O.V. Balachova, M.A.R. Alves, J.W. Swart, E.S. Braga, L. Cescato, CF4 plasma etching of materials used in microelectronics manufacturing, Microelectron. J. 31 (2000) 213–215, https://doi.org/10.1016/S0026-2692(99)00140-8.

[66] M.A.R. Alves, O. Balachova, E. Da Silva Braga, L. Cescato, Selective deposition of amorphous hydrogenated carbon films used as masks for reactive ion etching of Si using CF4, Vacuum 52 (1999) 313–314, https://doi.org/10.1016/S0042-207X(98)00305-4.

[67] K.A. Pears, J. Stolze, Carbon etching with a high density plasma etcher, Microelectron. Eng. 81 (2005) 7–14, https://doi.org/10.1016/j.mee.2005.02.002.

[68] M. Kakuchi, M. Hikita, T. Tamamura, Amorphous carbon films as resist masks with high reactive ion etching resistance for nanometer lithography, Appl. Phys. Lett. 48 (1998) 835, https://doi.org/10.1063/1.96683.

[69] J. Li, Y. Kim, S. Han, H. Chae, Ion-enhanced etching characteristics of sp2-Rich hydrogenated amorphous carbons in CF_4 plasmas and O_2 plasmas, Mater 14 (2021), https://doi.org/10.3390/ma14112941, 2941 14, 2941 (2021.

[70] J. Li, S.J. Kim, S. Han, Y. Kim, H. Chae, Etching characteristics of hydrogenated amorphous carbon with different sp2/sp3 hybridization ratios in CF4/O2 plasmas, Plasma Process. Polym. 18 (2021), 2100075, https://doi.org/10.1002/ppap.202100075.

[71] US6939794B2, Boron-doped amorphous carbon film for use as a hard etch mask during the formation of a semiconductor device - Google Patents. https://patents.google.com/patent/US6939794B2/en.

[72] S.W. Kim, M. Seol, Y. Cho, K.W. Shin, D. Lee, S.J. Jeong, et al., Graphene-based etch resist for semiconductor device fabrication, ACS Appl. Nano Mater. 3 (2020) 4635–4641, https://doi.org/10.1021/acsanm.0c00658.

[73] T. Matsumoto, T. Homma, Effect on etch rate and surface Roughness of crystal orientation of polycrystalline silicon used for consumable parts of reactive ion etching equipment, ECS J. Solid State Sci. Technol. 11 (2022), 084007, https://doi.org/10.1149/2162-8777/ac8832.